Research Article

# Continuous wavelet transformation of seismic data for feature extraction

Amjad Ali[1] · Chen Sheng-Chang[1] · Munawar Shah[2]

## Abstract

Continuous wavelet transformation (CWT) as a new mathematical tool has provided deep insights for the identification of localized anomalous zone in the time series data set. In this study, a three-layer geological model is investigated by CWT to locate seismic reflections temporally and spatially. This model consists of three layers, where the third layers of the anticline structure are assumed to act as a pure sandstone hydrocarbon reservoir with 10% porosity. The equation of Gassmann has been implemented for the pore fluid substitution in the reservoir. Synthetic seismic data are generated for the three-layer geological model. Due to the presence of noise, it is always difficult to interpret seismic data. But, CWT has the ability of noise reduction, improving the visualization of a data set and locating the anomalies in terms of scalogram and 3D CWT coefficients. Synthetic seismic data of the geological structure are transformed by CWT. The successful transformation of P-wave velocity, synthetic seismic data and acoustic impedance inversion provided evidence to distinguish different interfaces accurately. CWT has successfully located seismic reflections by localizing high-energy spectrum within the cone of influence. Three high-energy spectrums have been identified at 0.8 s, 1 s and 1.07 s, and it exactly matches the seismic data and three-layer geological model.

**Keywords** Gassmann's equation · P-wave velocity · Synthetic seismic trace · Acoustic impedance inversion · Continuous wavelet transformation

## 1 Introduction

Seismic reflection data are non-stationary in nature, because of their frequency variation with time. The geo-scientist has great interests in the trends and periodicities generated by complex subsurface geological structures. Generally, the Fourier transform is used to study these trends and periodicities in the geophysical time series. It is a mathematical tool that breaks down a time series signal into its component frequencies. Therefore, Fourier transform is a mathematical depiction of signal amplitudes of discrete components that construct it. Frequency-domain representation of the signal and the process of transformation from time to frequency domain are called

Fourier transform [28]. Initially, Fourier transform was first introduced for spatial fringe pattern analysis [22, 23]. It has been mainly implemented profilometry [24] and for the measurement of wave front shape [25]. But in Fourier transform, it has been assumed that the underlying processes in the geophysical time series are stationary. There are various techniques have been used to analyze the non-stationary time series signal. For time–frequency mapping, [11] illustrated the data-adaptive method and [5] implemented the short-time Fourier transform. The spectral decomposition of the seismic signal has also been used to delineate the subsurface response in terms of time-dependent frequency. To resolve the incised valley, Peyton et al. [19] used spectral decomposition along

✉ Amjad Ali, aali@zju.edu.cn; Chen Sheng-Chang, chenshengc@zju.edu.cn; Munawar Shah, munawar.shah@mail.ist.edu.pk | [1]School of Earth Sciences, Zhejiang University, Hangzhou City, Zhejiang Province, China. [2]Institute of Space Technology, Islamabad, Pakistan.

with coherency. For reservoir characterization, Partyka et al. [18] applied window spectral analysis to generate discrete frequency cubes, while [4] has used the matching pursuit algorithm for instantaneous spectral analysis to distinguish the low-frequency shadow underneath the reservoir.

Generally, in signal processing, for feature extraction, we are mainly interested to transform the signal in time and frequency domains simultaneously. For this purpose, the Fourier analysis is used, but it does not generate the actual time history of frequency variation when the frequency components are changing in the time domain. The Fourier transformation $F(\omega)$ of a time series signal $S(t)$ is given below:

$$F(\omega) = \int_{-\infty}^{\infty} S(t) \exp(-2\pi jft)dt \qquad (1)$$

Fourier transform of a time series signal is inner product between the given signal and basis function ($\exp(-2\pi jft)$), and t represents the time. Fourier analysis is unable to detect any local variation in the time domain. Therefore, it is not ideal for non-stationary time signal analysis, while [7] provided a partial solution to solve this problem and it is known as short-time Fourier transformation (STFT). In STFT, Gabor utilized a short-duration fixed window to extract all frequencies content in that time window. Gabor's STFT with a fixed short window is given below:

$$X(\omega, \tau) = \int_{-\infty}^{\infty} x(t)w(t - \tau) \exp(-i\omega t)dt \qquad (2)$$

But the major problem of Gabor's STFT is that it has a fixed window followed by fixed frequency. Due to this, fixed frequency enables only short and fixed time–frequency resolution.

Wavelet transformation (WT) is a new mathematical tool to identify the localized variations within a time series [14]. This provides a timescale spectrum instead of the time–frequency spectrum [20]. WT is a powerful technique to analyze random oscillation in a time series data set [9]. Continuous wavelet transform (CWT) is a subclass of wavelet transformation and it is mostly used for feature extraction from time series. The idea of CWT was derived from [7] short-time Fourier transform (STFT), where he fixed the time duration window to extract all the frequencies within the window.

Klausner et al. [12] have discussed in detail the application of CWT to address different issues, e.g., data availability and quality, database gaps and error points. In order to acquire high-quality delineation of data, Yi et al. [29] presented two normalizations for estimation of CWT. Adhikari

[1] did a study for characterization of a signal in terms of time and scale. Tian et al. [26] has successfully integrated Mann Kendal test and CWT to assess the sediment load and runoff variations in Yellow River, China. Palupi [17] used the CWT for the prediction of depth of different minerals in the mineral-rich Pacitan East, Java, Indonesia. Costa and Santos [6] implemented the CWT on standard precipitation index for the characterization of droughts in Sao Francisco river catchment. Zhou et al. [10] did a comparative study between Morlet and Pethat wavelets using CWT for singularity and damage detection.

The basic idea behind CWT is the wavelet implementation as a band-pass filter to the time series signal. This causes the translation and dilation of the mother wavelet. CWT can expand a time series in the time and frequency domains at the same time. Therefore, CWT can examine and find a localized anomaly in time series analysis distributed at equal intervals. The equation of CWT of a signal $f(t)$ at scale '$a$' and time '$b$', is given below:

$$W(a,b) = \int_{-\infty}^{\infty} f(t)\frac{1}{\sqrt{a}}\psi * \left(\frac{t-b}{a}\right)dt \qquad (3)$$

where $\psi(t)$ is the CWT and called mother wavelet, *is the complex conjugate, $W(a, b)$ are CWT coefficients. Here, '$a$' and '$b$' are translation and dilation parameters, respectively. The small values of '$a$' cause the mother wavelet contracted, and it produces high-frequency functions, while high values of '$a$' cause the mother wavelet stretched, and it produces low-frequency functions. Since the wavelet of CWT is not entirely localized, it has some edge artifacts and Torrence and Compo [27] called it the cone of influence (COI).

In this study, we are going to implement continuous wavelet transformation on 1D and 2D synthetic seismic data and on seismic attributes like P-wave velocity and acoustic impedance inversion (AI) to characterize different seismic interfaces. Particularly, the characterization of pore fluid contact in the reservoir through continuous wavelet transformation using only seismic data will be a good tool to develop new fields, where the geoscientists do not have the well log data. This can help the exploration geoscientists in decision making for exploring new areas and determining new well location.

## 2 Methodology

In this study, continuous wavelet transformation (CWT) is implemented on the P-wave velocity, AI and the synthetic seismic data of a geological model composed of three layers. In this model, the third layer acts as a pure sandstone

reservoir with 10% porosity. Whereas the uppermost part of the reservoir is hydrocarbon-saturated, the lower part is the brine water zone. Similarly, the second layer is shale and it is the cap rock for reservoir and first layer initiate from the surface to apex of second layer, as shown in Fig. 1.

The elastic and seismic properties of two distinct pore fluids (gas and brine water) have been computed using Baztle and Wang [2] equations. Next, the equation of Gassmann has been utilized for pore fluid substitution in the hydrocarbon reservoir. Then 2D synthetic seismic data are generated for the geological model using the Finite difference method (Fig. 2). Finally, the synthetic seismic data have been transformed using CWT in order to locate different seismic interfaces.
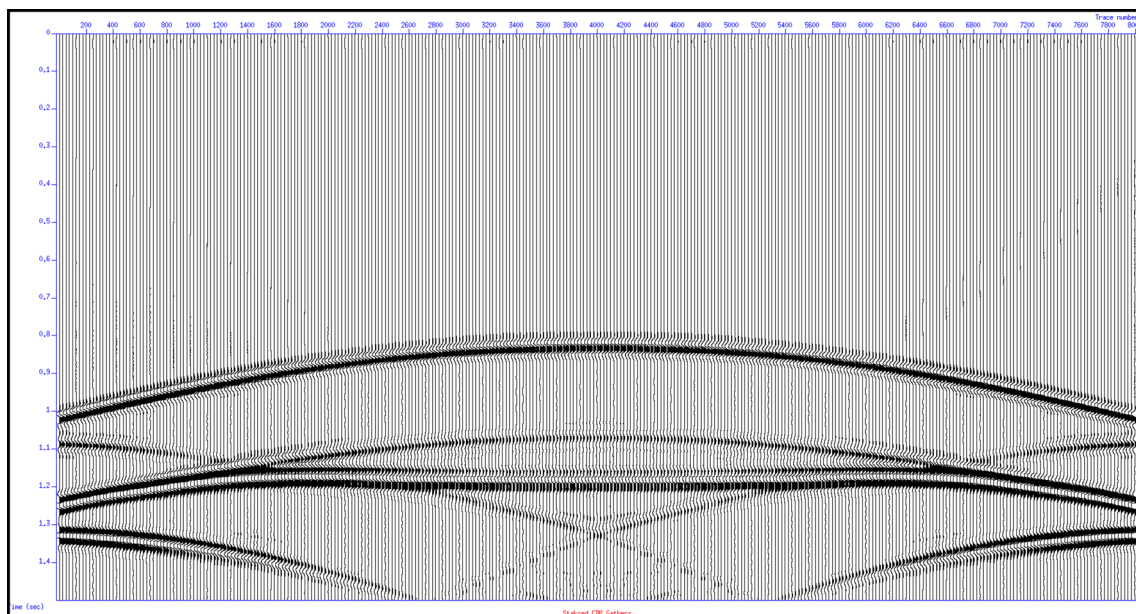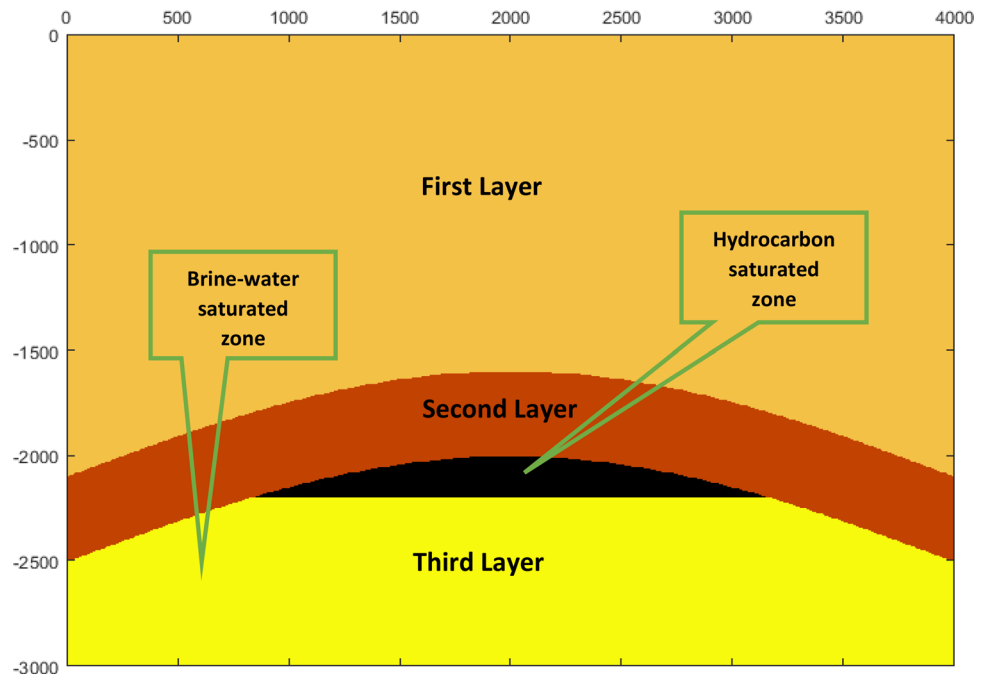
**Fig. 1** Three-layer geological model



**Fig. 2** 2D seismic data of the three-layer geological model

## 2.1 Fluid Properties

In this study, two different fluids have been used as pore fluids in the hydrocarbon reservoir, gas and brine water-bearer zones. At the first stage of this study, gas and brine's seismic and elastic properties are determined by implementing Baztle and Wang [2] equations. Then, for pore fluid substitution, the equation of Gassmann has been implemented to validate the anomalous zone. The computation of pore fluid properties is explained below.

## 2.2 Reservoir's Gas Properties

In this study, methane is used as a hydrocarbon pore fluid substitution in the reservoir. To determine the gas density, at first, the Kelvin equation is exercised to compute absolute temperature as:

$$T_{abs} = T + 273 \tag{4}$$

Here, $T_{abs}$ and T are the absolute temperature in Kelvin and the reservoir temperature in °C and it is 150 °C (assumed), respectively. Then, the water gradient equation is used to compute the pressure at the reservoir level:

$$P = ((D * 0.433) + 14.7) * 0.006894757293178 * 3.28 \tag{5}$$

Here, $P$ and $D$ are pressure in psi and depth in m, respectively. Then, to compute the pseudo-pressure and temperature, the following equations of Batzle and Wang [2] are used:

$$P_r = \frac{P}{4.892 - 0.4048 * G} \tag{6}$$

$$T_r = \frac{T_{abs}}{94.72 + 170.75 * G} \tag{7}$$

$T_r = \frac{T_a}{94.72 + 170.75 * G}, T_r = \frac{T_a}{94.72 + 170.75 * G}, T_r = \frac{T_a}{94.72 + 170.75 * G}$ Here, $G$ is the gas-to-oil ratio and for methane, it is 0.56.

Then, the gas density is calculated as [2]:

$$\rho_g = \frac{28.8 \, GP}{ZRT_{abs}} \tag{8}$$

Here, $\rho_g$ and $R$ are gas density in g/cm$^3$ and gas constant ($R = 8.31441$ Jg$^{-1}$/mol deg), respectively, and $Z$ is evaluated as [2]:

$$Z = aP_r + b + cd \tag{9}$$

Here,

$$a = 0.03 + 0.00527(3.7 - T_r)^3 \tag{10}$$

$$b = 0.642T_r - 0.007T_r^4 - 0.52 \tag{11}$$

$$c = 0.109(3.85 - T_r)^2 \tag{12}$$

$$d = EXP\left\{-\left[0.45 + 8 * \left(0.56 - \frac{1}{T_r}\right)^2\right]\frac{P_r^2}{T_r}\right\} \tag{13}$$

Finally, the gas bulk modulus is determined as [2]:

$$K_g = \frac{P\gamma}{1 - \frac{P_r}{Z}f} \tag{14}$$

Here,

$$\gamma = 0.85 + \frac{5.6}{P_r + 2} + \frac{27.1}{(P_r + 3.5)^2} - 8.7e^{-0.65(P_r+1)} \tag{15}$$

$$f = cdm + a \tag{16}$$

$$m = 1.2 * \left\{-\left[0.45 + 8 * \left(0.56 - \frac{1}{T_r}\right)^2\right]\frac{P_r^{0.2}}{T_r}\right\} \tag{17}$$

In Table 1, all the results of the above equations are arranged.

## 2.3 Reservoir's Brine water properties

Initially, brine water density is calculated as [2]:

$$\rho_b = \rho_w + S\{0.668 + 0.44S + 10^{-6}$$
$$[300P - 2400P * S + (80 + 3T - 3300S - 13P + 47P * S)]\} \tag{18}$$

Here, $\rho_b$ is brine water density in (g/cm$^3$), $\rho_w$ is the freshwater density of 1 g/cm$^3$, $S$ is salinity with 84,000 PPM (assumed), and $T$ and $P$ are temperature and pressure, respectively.

Table 1 Gas-computed elastic and seismic properties

| S/No. | Property | Computed value |
|---|---|---|
| 1 | Pressure (MPa) | 21.160 |
| 2 | Tabs (K) | 423.150 |
| 3 | $T_r$ (K) | 2.2232 |
| 4 | $P_r$ (MPa) | 4.5357 |
| 5 | $Z$ | 0.9857 |
| 6 | $\rho_g$ (g/cm$^3$) | 0.0945 |
| 7 | m | −0.3995 |
| 8 | $\gamma$ | 10.377 |
| 9 | $f$ | 0.01203 |
| 10 | $K_g$ (Pascal) | 21,960 |

Brine water velocity is calculated as [2]:

$$V_b = V_F + S(1170 - 9.6T + 0.055T^2 - 8.5 \times 10^{-5}T^3 + 2.6P - 0.0029TP - 0.0476P^2)$$
$$+ S^{1.5}(780 - 10P + 0.16P^2) - 1820S^2 \qquad (19)$$

Here, $V_b$ and $V_w$ are brine water velocity and freshwater velocity, respectively. Freshwater velocity is determined as [2]:

$$V_w = \sum_{i=0}^{4} \sum_{j=0}^{3} w_i T^i P^i \qquad (20)$$

The $w_{ij}$ coefficients are given below:

$w_{00} = 1402.85 \quad w_{02} = 3.437 \times 10^{-3}$

$w_{10} = 4.871 \quad w_{12} = 1.739 \times 10^{-4}$

$w_{20} = -0.04783 \quad w_{22} = -2.135 \times 10^{-6}$

$w_{30} = 1.487 \times 10^{-4} \quad w_{32} = -1.455 \times 10^{-8}$

$w_{40} = -2.197 \times 10^{-7} \quad w_{42} = 5.230 \times 10^{-11}$

$w_{01} = 1.524 \quad w_{03} = -1.197 \times 10^{-5}$

$w_{11} = -0.0111 \quad w_{13} = -1628 \times 10^{-6}$

$w_{21} = 2.747 \times 10^{-4} \quad w_{23} = 1.237 \times 10^{-8}$

$w_{31} = -6.503 \times 10^{-7} \quad w_{33} = 1.327 \times 10^{-10}$

$w_{41} = 7.987 \times 10^{-10} \quad w_{43} = -4.614 \times 10^{-13}$

Finally, the brine water fluid bulk modulus is computed as:

$$K_b = (\rho * V_p)/10^6 \qquad (21)$$

The outputs of the above equations are listed in Table 2.

# 3 Gassmann's equation

The equation of Gassmann is an established equation for fluid substitution to examine seismic properties variations. Gassmann's equation for saturated rock bulk modulus is defined as:

$$K_s = K_d + \frac{\left(1 - {K_d}/{K_m}\right)^2}{\frac{\emptyset}{K_f} + \frac{1-\emptyset}{K_m} - \frac{K_d}{K_m^2}} \qquad (22)$$

Here, in this study, reservoir rock is pure sandstone; according to published data, matrix bulk modulus ($K_m$) of sandstone is 36.6 GPa (Mavko et al.). $K_d$ and $\mu_d$ are dry rock bulk modulus and shear modulus, respectively. They are calculated using critical porosity equations of Nur et al. [15] as: For $K_d$,

$$K_d = K_m\left(1 - \frac{\emptyset}{\emptyset_c}\right) \qquad (23)$$

For $\mu_d$,

$$\mu_d = \mu_m\left(1 - \frac{\emptyset}{\emptyset_c}\right) \qquad (24)$$

Here, $\emptyset$ is reservoir porosity and it is 10%, whereas it is the critical porosity of sandstone and it is 40% [15]. The density log equation has been used to compute the saturated rock density for gas and brine water as:

$$\rho_s - (1 - \emptyset)\rho_m + \emptyset\rho_f \qquad (25)$$

Finally, saturated rock's velocity is computed as:

$$V_p = \sqrt{\frac{K_s + 4/3\mu_s}{\rho_s}} \qquad (26)$$

The outputs of the above equations for gas and brine water are listed in Table 3.

Table 2 Brine water-computed elastic and seismic properties

| S/No. | Property | Computed value |
|---|---|---|
| 1 | $S$ (PPM) | 84,000 |
| 2 | $\rho_b$ (g/cm$^3$) | 1.0595 |
| 3 | $V_b$ (m/sec) | 1499 |
| 4 | $K_b$ (Pascal) | $2.3775 * 10^9$ |

Table 3 Computed parameters of brine and gas using Gassmann's equation

| S/No. | Property | Gas Value | Brine Value |
|---|---|---|---|
| 1 | $\rho_s$ (Kg/m$^3$) | 2139 | 2332 |
| 2 | $\mu_d$ (Pascal) | $2.99 * 10^{10}$ | $2.99 * 10^{10}$ |
| 3 | $K_d$ (Pascal) | $2.74 * 10^{10}$ | $2.74 * 10^{10}$ |
| 4 | $K_s$ (Pascal) | $2.74 * 10^{10}$ | $2.60 * 10^{10}$ |
| 5 | $V_p$ (m/sec) | 4344 | 4963 |

## 4 Inversion and wavelet transformation

In this paper, the synthetic seismic data are generated for the geological model, using each layer's velocity and density. Then, P-wave velocity and acoustic impedance (AI) are computed from seismic data. The interval velocity is computed using Dix's equation. Recursive inversion method of Becquey et al. [3] has been used for AI inversion,

$$AI_i = AI_z \frac{1 + k_i}{1 - k_i} \tag{27}$$

Here, is the final product of AI inversion, is the acoustic impedance of the first layer and this must be known, and is the reflection coefficient of each reflector.

CWT has emerged with the localization concept of the filtering function of Gabor [7]. The main objective of CWT transformation is to recognize the local anomalies for feature extraction in the time series data set. CWT has the ability to expand a time series into a time–frequency domain at the same time. Therefore, CWT can examine and find a localized anomaly in time series analysis distributed at equal intervals. In this study, CWT has been adopted to identify and confirm seismic reflections as a localized anomaly. To localize the anomalous zones, 'Haar' wavelet has been used as a mother wavelet because it can detect sudden discontinuities and abrupt changes in the time series analysis. Haar wavelet is a string of rescaled squared shape functions which form orthonormal wavelet basis. There are two functions: Scaling function and mother wavelet play an important role in wavelet analysis. Scaling function of Haar wavelet is defined as:

$$\emptyset(x) = \begin{cases} 1, & \text{if } 0 \le < 1 \\ 0, & \text{otherwise} \end{cases} \tag{28}$$

The mother wavelet of Haar wavelet can be defined as:

$$\psi(x) = \begin{cases} 1, & 0 \le x < 1/2 \\ -1, & 1/2 \le x < 1 \\ 0, & \text{otherwise} \end{cases} \tag{29}$$

The analysis is presented in the form of scalogram and 3D CWT coefficients.

## 5 Results

In this study, the three-layer geological model is used to observe different seismic variations through statistical and CWT. As discussed before, the third layer of this model acts as a reservoir in the constituted model using Gassmann's equation. The uppermost part of the reservoir is gas-saturated, and subsequently, lower part is the brine water-saturated zone. The objective of this study is feature extraction by CWT application. Initially, 5% Gaussian noise is added to compute P-wave velocity, synthetic seismic data and acoustic impedance inversion. The signal-to-noise ratio (SNR) is −12 dB, the negative SNR means that noise power is higher than signal power and it makes this a more realistic scenario. Due to the presence of noise, it is hard to define precisely different zones and contacts in seismic data. But CWT has the ability of noise reduction, identification of different trends and recognition of discontinuities in a time series data set. After the computation of seismic data, P-wave velocity and AI inversion with 5% Gaussian noise, CWT is implemented to identify different zones and contacts by localizing the anomalous zone in time series data set in the form of scalogram and 3D CWT coefficients.

### 5.1 P-wave velocity

In this paper, P-wave velocity is computed from seismic for the geological model of this study. Then, 5% Gaussian noise is added to P-wave velocity to make it more realistic and applicable in the real world and CWT is applied to P-wave velocity. In Fig. 3, one can see 2D scalogram as a function of time and wavelet sampling period with a cone of influence (COI). The white dashed line is representing the COI as variation in mother wavelet. Within COI, the results provided by CWT are reliable and accurate, while beyond this line, the wavelet has been stretched outside the observational interval and it is affected by edge effect artifacts. Within the COI of CWT of P-wave velocity, three high-energy spectrums are identified and they are concentrated at three different points on timescale, i.e., 0.8 s, 1 s and 1.07 s. The first region of high-energy spectrum represents the contact between the first layer and the second layer at 0.8 s, second region of high energy represents the contact between second layer (shale) and third layer (sandstone reservoir) at 1 s and the third region is the contact between hydrocarbon-saturated zone and brine water-saturated zone within the reservoir at 1.07 s.

Furthermore, we showed variation in P-wave velocity for single trace and for the whole 2D seismic data by 3D CWT and it exhibits a sequence of better results in order to identify different boundaries and contacts (Fig. 3). Due to the abrupt changes in time series, CWT generates large wavelet coefficient values at the points of sudden transitions. Therefore, 3D representation of CWT wavelet coefficients generates better visualization for the interpretation of time series and it provides a better result for the identifications of different contacts. Besides negative SNR, three clear boundaries in terms of time slices of CWT coefficients have been identified at 0.8 s, 1 s and 1.07 s (Fig. 3).

**Fig. 3** Continuous wavelet transformation of P-wave velocity with 'Haar' wavelet **a** scalogram and **b** CWT of single-trace P-wave velocity, while **c** is the 3D CWT of P-wave velocity model of the three-layer geological model
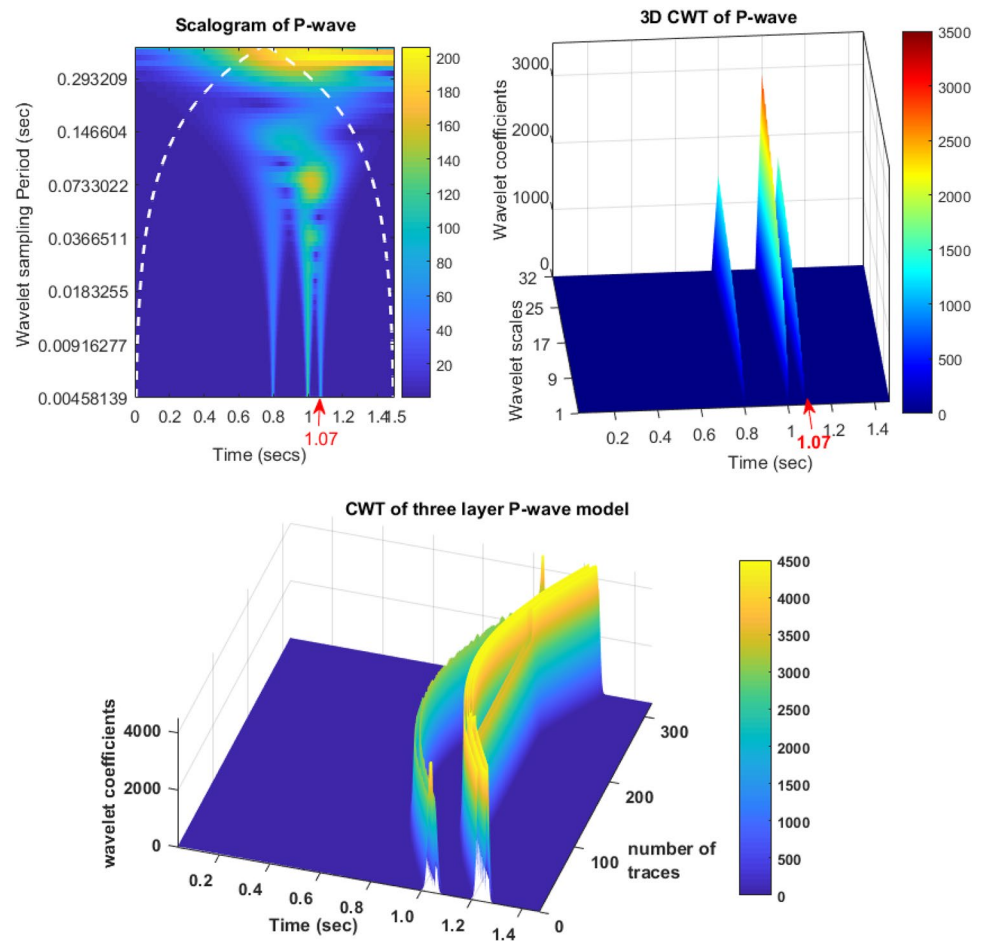


In this study, the third high-energy spectrum represents the pore fluid contact in the reservoir, as it is pointed with a red arrow in Fig. 3.

## 5.2 Synthetic seismic trace

In order to provide more stringent proof and evidence, a synthetic seismic trace is generated using [16] conventional model. The acoustic impedance was computed using the P-wave velocity and density model, and then, zero-phase wavelet is convolved with acoustic impedance to get the seismic trace, and finally, Gaussian noise is added to synthetic trace (Fig. 4). This synthetic seismic trace with noise in the middle of the geological model has been used for CWT to identify different interfaces.

Figure 5 shows the CWT of seismic trace in the form of 2D and 3D scalogram representation, respectively. Within the COI of scalogram of synthetic seismic trace, three high-energy spots are identified and it is effectively concentrated at three different points of timescale at 0.8 s, 1 s and 1.07 s. These high-energy spots represents: The first region is the contact between first layer and second layer at 0.8 s, the second region of high energy represents the

contact between second layer (shale) and the third layer (sandstone reservoir) at 1 s and the third region is the contact between hydrocarbon-saturated zone and brine water within the reservoir at 1.07 s, as shown in Fig. 5.

Similarly, the CWT of seismic trace exhibits much better results in the form of a 3D plot (Fig. 5). This presents better visualization of CWT coefficients for the interpretation of a time series. Apart from the noise addition in the seismic trace, three significantly high-energy spectrums of CWT coefficients can be easy to distinguish at 0.8 s, 1 s and 1.07 s (Fig. 6). In this study, the third high-energy spectrum represents the pore fluid contact in the reservoir, as it is pointed with a red arrow in Fig. 5. They are exactly at the same point in time as these were assumed in the three-layer geological model.

Furthermore, we showed variation in 2D synthetic seismic data as 2D and 3D CWT and it exhibits a sequence of better results in order to identify different boundaries and contacts (Fig. 6c). 2D and 3D representation of CWT produced better visualization for the interpretation of seismic data and it provides a better result for the identifications of different contacts. Besides negative SNR, three clear boundaries in terms of time slices of CWT coefficients have
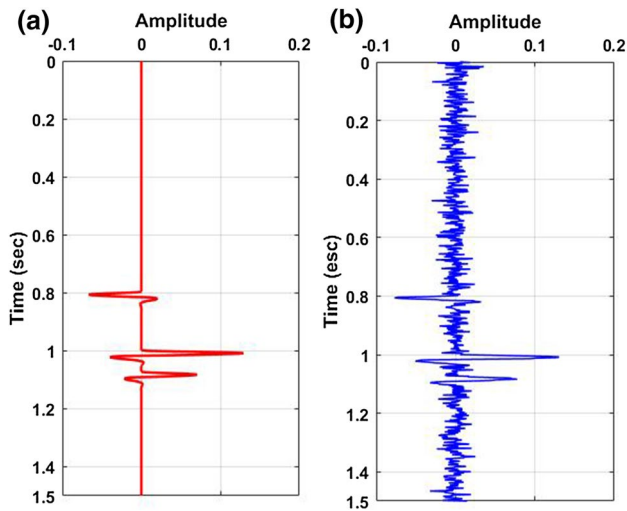
**Fig. 4** Synthetic seismic trace at the middle of the geological model **a** without noise, **b** with 5% Gaussian noise

been identified at 0.8 s, 1 s and 1.07 s (Fig. 6c). In this study, the third high-energy spectrum represents the pore fluid contact in the reservoir.

## 5.3 Acoustic impedance inversion (AI)

The recursive inversion method of Becquey et al. [3] has been used for AI inversion (Fig. 7). In this study, Fig. 7a shows AI inversion without any noise addition to seismic trace. All the contacts are prominent and they can be easily marked with significant accuracy. Similarly, Fig. 7b shows AI inversion after the Gaussian noise addition to the seismic trace. The second and third interface is not clear as in the case of previous analysis (Fig. 7a).

In order to identify the seismic interfaces accurately, CWT is adopted on the AI noisy data. Figure 8 shows a 2D scalogram as a function of time and wavelet sampling period with COI of the single seismic trace. Within the COI of a wavelet transformation of AI, three significant spectrums are identified at 0.8 s, 1 s and 1.07 s. Due

**Fig. 5** Wavelet spectrum of synthetic seismic trace with 5% Gaussian noise using 'Haar' wavelet, **a** scalogram, **b** CWT of synthetic seismic trace; the fluid contact is marked by red circle at 1.07 s
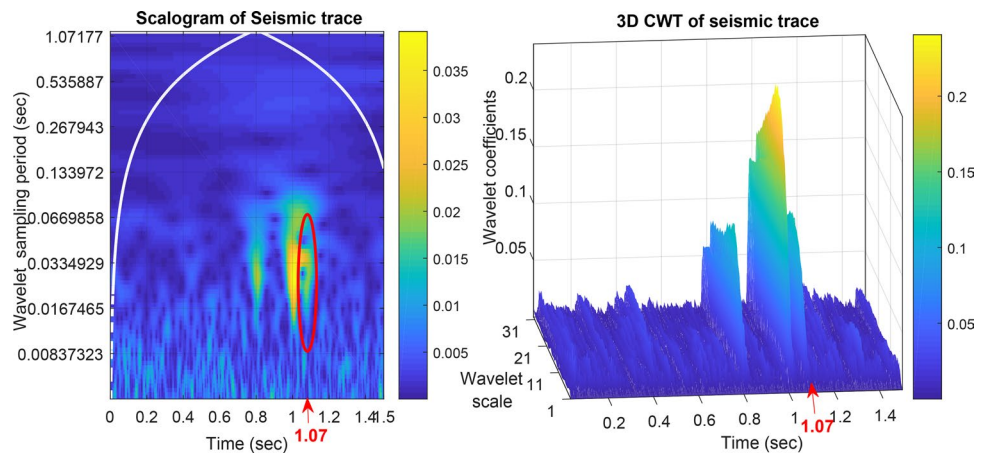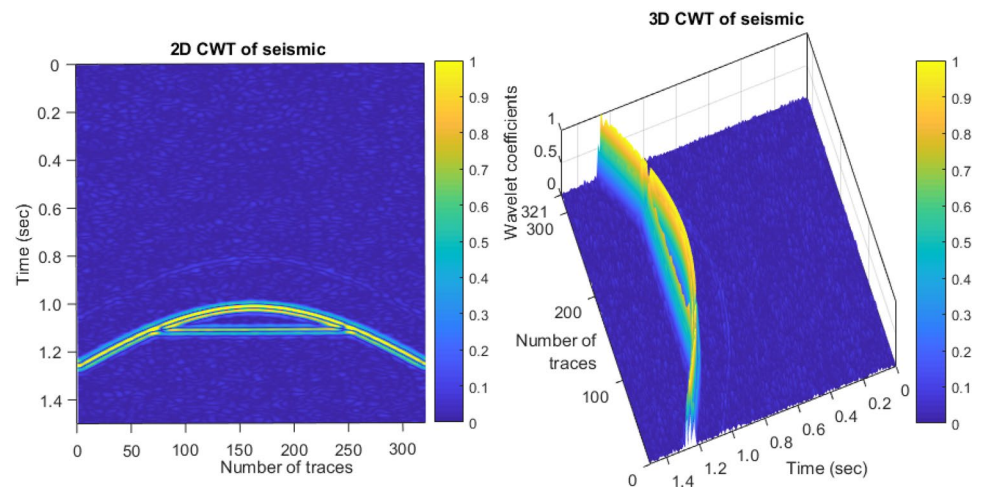


**Fig. 6** Continuous wavelet transformation of 2D seismic data of the three-layer geological model with 5% Gaussian noise, **a** 2D and **b** 3D representation of CWT of seismic data
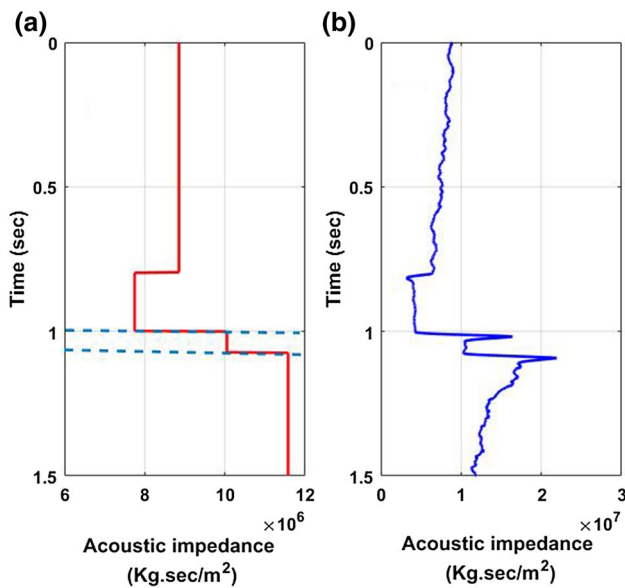
**Fig. 7** Acoustic impedance inversion using Becquey et al. [3]. **a** Without noise, **b** with 5% Gaussian noise

to small-time separation between the second layer and third layer, the second and third high-energy spectrums are overlapping on each other (i.e., Figure 8). The second high-energy spectrum represents the contact between the shale (second layer) and sandstone (third) of the geological model. On the other hand, third high-energy spectrum is pore fluid contact between the hydrocarbon-saturated zone and brine water-saturated zone within the reservoir.

Furthermore, we showed variation in AI inversion for single trace and for the whole 2D seismic data by 3D CWT and it exhibits a sequence of better results in order to identify different boundaries and contacts (Fig. 8). Due to the abrupt changes in time series analysis, CWT generates large wavelet coefficient values at points of immediate transitions between different strata. Therefore, 3D representation of CWT wavelet coefficients generates better visualization for the interpretation of a time series of AI for the three-layer model. Besides the presence of negative SNR, three clear boundaries can be explicitly identified by CWT analysis. These prominent anomalous zones can be seen at 0.8 s, 1 s and 1.07 s, as it was anticipated in the previous investigation in this study.

**Fig. 8** Continuous wavelet transformation of acoustic impedance inversion with 'Haar' wavelet (**a**) scalogram and (**b**) CWT of single-trace AI inversion, while (**c**) is the 3D CWT of AI inversion of 2D seismic data of the three-layer geological model
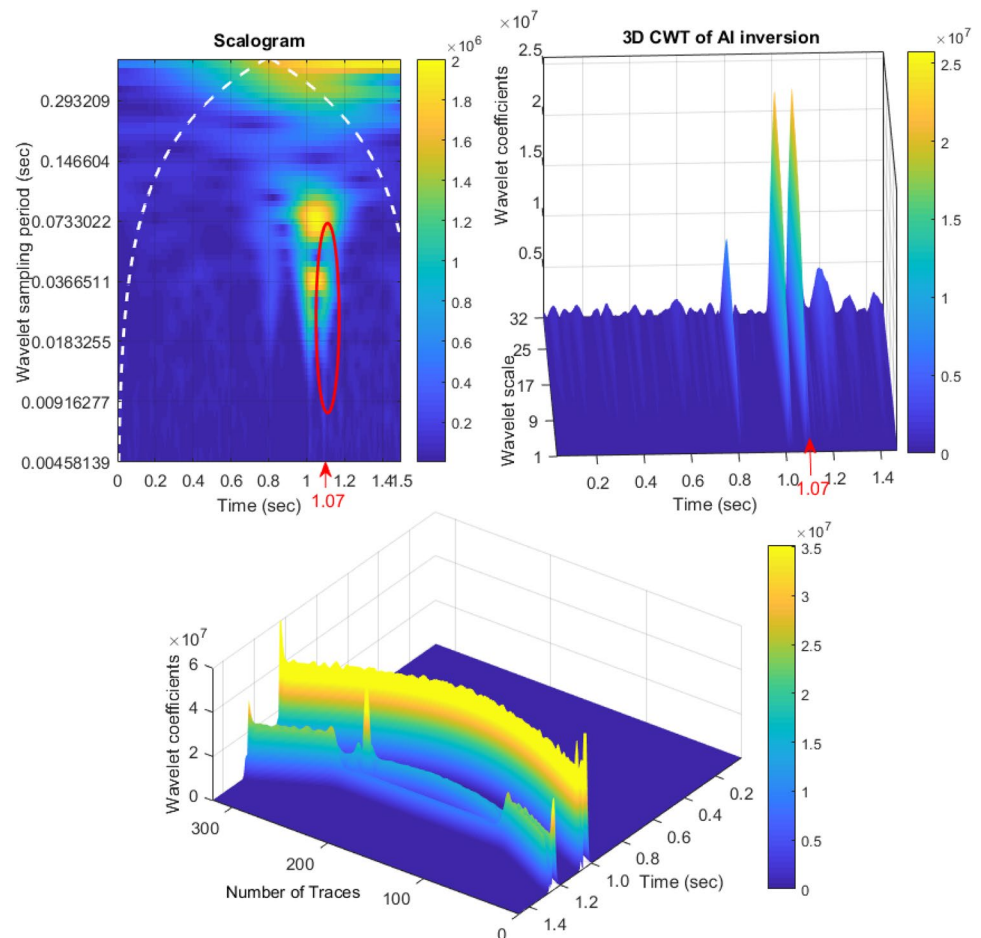
**Table 4** Comparative results between convolution and CWT technique

| Method | Equation | Comparison | |
|---|---|---|---|
| Convolution | $y(t) = g(t) * f(t) + \text{noise}$ | Seismic Trace | |
| | | Peaks | |
| | | 0.8 s | |
| | | 1.0 s | |
| | | 1.07 s | |
| Continuous wavelet transformation | $W(a,b) = \int\limits_{-\infty}^{\infty} f(t)\frac{1}{\sqrt{a}}\psi * \left(\frac{t-b}{a}\right)dt$ | Seismic signal with noise | |
| | | Scalogram | 3D coefficients |
| | | Bright spots | High-energy spectrums |
| | | 0.8 s | 0.8 s |
| | | 1.0 s | 1.0 s |
| | | 1.07 s | 1.07 s |
| | | P-wave velocity | |
| | | Scalogram | 3D coefficients |
| | | Bright spots | High-energy spectrums |
| | | 0.8 s | 0.8 s |
| | | 1.0 s | 1.0 s |
| | | 1.07 s | 1.07 s |
| | | Acoustic Impedance Inversion | |
| | | Scalogram | 3D coefficients |
| | | Bright spots | High-energy spectrums |
| | | 0.8 s | 0.8 s |
| | | 1.0 s | 1.0 s |
| | | 1.07 s | 1.07 s |



**Fig. 9** Normalized CWT coefficients of P-wave velocity, seismic trace, acoustic impedance and seismic trace along with confidence bounds
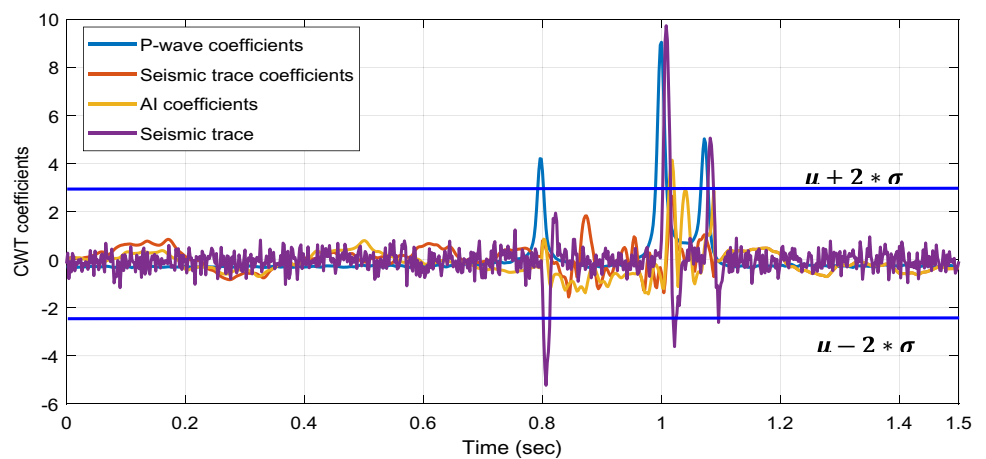
At the end of the CWT study, in order to analyze the ability to recognize different seismic interfaces in the presence of noise by two different methods, a comparative study between convolution method and CWT technique has been added, as shown in Table 4. This shows that CWT is a powerful tool to identify different seismic reflectors using seismic data and seismic attributes. Besides that, the statistical study is also carried out in terms of confidence bound with a 95% interval for normalized CWT coefficients of P-wave velocity, seismic trace, acoustic impedance and synthetic seismic trace, as shown in Fig. 9. At three different points on the timescale, the CWT coefficients are stand out of the upper and lower bounds as anomalous zones, at 0.8 s, 1 s and 1.07 s. This also validates the results of the continuous wavelet transformation of P-wave velocity, seismic trace and acoustic impedance.

## 6 Discussion

Here, we discuss the implementation of CWT in order to identify different seismic reflections from different interfaces. Several examples have been cited using wavelets transform by Gurley and Kareem [8] in order to identify and characterize in the fields of wind, ocean engineering and earthquakes. This includes the spectral analysis for the identification of transient events, simulation of non-stationary signals and noise reduction. CWT can be used to interpret seismic data in time and frequency domain simultaneously. For the detection of hydrocarbon, Sun et al. [21] implemented the instantaneous spectral analysis hinge on matching pursuit decomposition. But Mallet and Zhang [13] explained that matching pursuit decomposition separates the given signal structure that is consistent as regards to the given wavelet. However, if the given signal is combination of several fundamental dictionaries, then it will be hard to select a specific one to study a non-stationary signal. CWT of a non-stationary time series data is accomplished by a mother wavelet. This technique gives better resolution and visualization of data. We have transformed the seismic data and it attributes with 5% Gaussian noise using CWT and presented as scalogram and three-dimensional coefficients. CWT has the ability of noise reduction, identification of different trends and recognition of discontinuities in a non-stationary time series data set. Scalogram has been acquired by windowing the time series with scaling and shifting in time of mother wavelet. Due to the scaling and shifting in time, the mother wavelet shrinks and stretches which produces high CWT coefficient values. The shrinking of mother wavelet produces high-frequency functions, and this is good to identify transient events. the stretching of mother wavelet produces low-frequency functions, and this is good to detect long duration of low-frequency events.

## 7 Conclusion

A large number of algorithms exist to identify different patterns in a non-stationary time series. In this study, we have implemented CWT on a non-stationary raw seismic data in order to localize and identify seismic reflections in a time–frequency domain. The CWT has the ability to expand a time series signal into time as well as frequency domain. The spectral decomposition of 1D seismogram into 2D scalogram and 3D CWT time slice is a great improvement in signal processing. It can separate different seismic events of different seismic frequencies and it can localize the events as anomalous zones. CWT mainly depends on the selection of mother wavelet as well as translation (a) and dilation (b) of the mother wavelet.

We have studied the three-layer geological model, where the third layers acted as a pure sandstone reservoir with 10% porosity. The equation of Gassmann has been used for pore fluid substitution, and synthetic seismic data with -12 dB SNR have been generated. Then, CWT has been implemented on seismic attributes like P-wave velocity, synthetic seismic trace and AI. The main outcomes of this study can be summarized as:

1. CWT is found as an effective tool for the identification of abrupt, sudden variations in time series seismic signals.
2. These abrupt changes and boundaries in times series data set outcomes with substantial big wavelet coefficient values are obtained.
3. These large wavelet coefficients are concentrated at a narrow region on timescale, known as the cone of influence. This COI is the indication and position of the transition in a time series data set.
4. Even in the presence of noise in the time-series signals, CWT successfully identifies all the boundaries of the proposed three-layer geological model.
5. The proper localization of the anomaly or abrupt change in a time series largely depends on the selection of mother wavelet, translation and dilation scale of CWT.
6. CWT can be implemented on seismic data as well as on seismic attributes for the confirmation of the final results of seismic inversion and attributes.

## Compliance with ethical standards

**Conflict of interest** On behalf of all authors, the corresponding author states that there is no conflict of interest.

## References

1. Adhikari B (2015) HILDCAA-related effects recorded in middle low latitude magnetometers. InstitutoNacional de PesquisasEspaciais, Sao Jose dos Campos
2. Batzle M, Wang Z (1992) Seismic properties of pore fluids. Geophysics 57(11):1396–1408. https://doi.org/10.1190/1.1443207
3. Becquey M, Lavergne M, Willm C (1979) Acoustic impedance logs computed from seismic traces. Geophysics 44(9):1485–1501. https://doi.org/10.1190/1.1441020
4. Castagna JP, Sun S, Siegfried RW (2003) Instantaneous spectral analysis: detection of low-frequency shadows associated with hydrocarbons. Lead Edge 22(2):120–127
5. Cohen L (1995) Time-frequency analysis. Prentice Hall, New York

6. Costa V, Santos M (2019) Time-space characterization of droughts in the São Francisco river catchment using the Standard Precipitation Index and continuous wavelet transform. RBRH. https://doi.org/10.1590/2318-0331.241920180092

7. Gabor D (1946) Theory of communication Part 1: the analysis of information. J Inst Electr Eng Part III Radio Commun Eng 93(26):429–441

8. Gurley K, Kareem A (1999) Applications of wavelet transforms in earthquake, wind and ocean engineering. Eng Struct 21(2):149–167

9. Holschneider M (1995) Wavelets. An analysis tool

10. Jie Zhou ZL, Chen Jiyue (2020) Singularity detection based on two dimensional continuous wavelet transform. J Image Signal Process 09:111–118. https://doi.org/10.12677/JISP.2020.92014

11. Jones DL, Baraniuk RG (1995) An adaptive optimal-kernel time-frequency representation. IEEE Trans Signal Process 43(10):2361–2371

12. Klausner V, Papa AR, Mendes O, Domingues MO, Frick P (2013) Characteristics of solar diurnal variations: a case study based on records from the ground magnetic station at Vassouras, Brazil. J Atmos Solar Terr Phys 92:124–136

13. Mallat S (1999) A wavelet tour of signal processing. Elsevier, Amsterdam

14. Mallat SG (1987) A theory for multiresolution signal decomposition: the wavelet representation

15. Nur AM, Mavko G, Dvorkin J, Gal D (1995) Critical porosity: the key to relating physical properties to porosity in rocks. SEG Technical Program Expanded Abstracts 1995 (pp. 878-881): Society of Exploration Geophysicists

16. Yilmaz O, et al. (2001) 1 Fundamentals of signal processing *seismic data analysis,* Society of Exploration Geophysicists, pp 25–158

17. Palupi IR (2018) Depth prediction of gravity data by using continous wavelet transform. Paper presented at the EAGE-HAGI 1st Asia Pacific Meeting on Near Surface Geoscience and Engineering

18. Partyka G, Gridley J, Lopez J (1999) Interpretational applications of spectral decomposition in reservoir characterization. Lead Edge 18(3):353–360

19. Peyton L, Bottjer R, Partyka G (1998) Interpretation of incised valleys using new 3-D seismic techniques: a case history using spectral decomposition and coherency. Lead Edge 17(9):1294–1298

20. Rioul O, Vetterli M (1991) Wavelets and signal processing. IEEE Signal Process Mag 8(4):14–38. https://doi.org/10.1109/79.91217

21. Sun S, Castagna JP, Siegfried RW (2002) Examples of wavelet transform time-frequency analysis in direct hydrocarbon detection. SEG Technical Program Expanded Abstracts 2002, Society of Exploration Geophysicists, pp 457-460

22. Takeda M (1990) Spatial-carrier fringe-pattern analysis and its applications to precision interferometry and profilometry: an overview. Ind Metrol 1(2):79–99

23. Takeda M, Ina H, Kobayashi S (1982) Fourier-transform method of fringe-pattern analysis for computer-based topography and interferometry. JosA 72(1):156–160

24. Takeda M, Mutoh K (1983) Fourier transform profilometry for the automatic measurement of 3-D object shapes. Appl Opt 22(24):3977–3982

25. Takeda M, Ru Q-S (1985) Computer-based highly sensitive electron-wave interferometry. Appl Opt 24(18):3068–3071

26. Tian S, Xu M, Jiang E, Wang G, Hu H, Liu X (2018) Temporal variations of runoff and sediment load in the upper Yellow River, China. J Hydrol. https://doi.org/10.1016/j.jhydrol.2018.10.033

27. Torrence C, Compo GP (1998) A practical guide to wavelet analysis. Bull Am Meteor Soc 79(1):61–78

28. Walker JS (1996) Fast fourier transforms. CRC Press, Boca Raton

29. Yi H (2014) High precision computation of morlet wavelet transform for multi-period analysis of climate data. J Inf Comput Sci. https://doi.org/10.12733/jics20104715